Physics of Fluids

RESEARCH ARTICLE | DECEMBER 26 2023

Sensitivity of acoustofluidic particle manipulation to microchannel height in standing surface acoustic wave-based microfluidic devices

Yiming Li (李一铭) ; Dongfang Liang (梁东方) ; Alexandre Kabla ; Yuning Zhang (张宇宁) ; Xin Yang (杨欣)

Physics of Fluids 35, 122018 (2023)
https://doi.org/10.1063/5.0177118

Physics of Fluids ARTICLE pubs.aip.org/aip/pof

Sensitivity of acoustofluidic particle manipulation to microchannel height in standing surface acoustic wave-based microfluidic devices

Cite as: Phys. Fluids **35**, 122018 (2023); doi: 10.1063/5.0177118
Submitted: 19 September 2023 · Accepted: 1 December 2023 ·
Published Online: 26 December 2023

View Online Export Citation CrossMark

Yiming Li (李一铭),[1] Dongfang Liang (梁东方),[1,a)] Alexandre Kabla,[1] Yuning Zhang (张宇宁),[2] and Xin Yang (杨欣)[3]

AFFILIATIONS

[1]Department of Engineering, University of Cambridge, Cambridge CB2 1PZ, United Kingdom
[2]Key Laboratory of Power Station Energy Transfer Conversion and System (Ministry of Education), School of Energy Power and Mechanical Engineering, North China Electric Power University, Beijing 102206, China
[3]School of Engineering, Cardiff University, Cardiff CF24 3AA, United Kingdom

[a)]Author to whom correspondence should be addressed: dl359@cam.ac.uk

ABSTRACT

In this paper, the flow and particle trajectories, induced by standing surface acoustic waves (SSAWs) in a poly-dimethylsiloxane microchannel, are investigated by establishing a two-dimensional cross-sectional model with the finite element method and improved boundary conditions. Extensive parametric studies are conducted regarding the channel height, ranging from 0.2 to 4.0 times the spacing of the repetitive vertical interference pattern, to investigate its influences on the flow field and microparticle aggregation. The first-order flow field is found to be related to the channel height, exhibiting a periodic spatial distribution and oscillatory variation in its amplitude as the height changes. We theoretically analyze the propagation mechanism of the acoustic waves in the vertical direction and thus determine the periodicity of the wave interference pattern. Furthermore, we find that the speed of the particle aggregation is a function of the channel height, so the channel height can be optimized to maximize the strength of the first-order flow field and thus minimize the time of particle aggregation. The optimum heights can reduce the aggregation time by up to 76%. In addition, the acoustophoretic motions of microparticles exhibit a spatially dependent pattern when the channel height becomes larger than a quarter of the wavelength of the SAW, which can be explained by the change in the ratio between the radiation force and the streaming drag force from position to position. Our findings provide guidelines to the design and optimization of SSAW-based acoustofluidic devices.

I. INTRODUCTION

Microfluidics has shown its promising potential for the manipulation of fluids and particles at a microscale.[1–6] Among the various techniques applied in microfluidics, acoustofluidics has gained significant attention recently due to its noninvasive and label-free nature.[7–12] In standing surface acoustic wave (SSAW)-based microfluidic devices, SSAW is formed on the surface of a piezoelectric substrate by the superposition of two counter-propagating SAWs emitted by a pair of interdigitated transducers (IDTs). Due to the scattering of the acoustic waves, particles suspended in the microchannel experience a net force that drives them toward the pressure nodes (PNs) or antinodes (ANs) depending on their acoustic properties. By tailoring the geometry of the microchannel and operating parameters such as frequency, intensity, and phase of the SAW, researchers can achieve selective manipulation of particles based on their size, density, or compressibility.[9,13–15]

The performance of the SSAW-based devices is significantly influenced by various factors,[16,17] including the device design (microchannel geometry, wall material, location of IDTs, etc.), operational parameters (frequency and amplitude of the SAW, flow rate, temperature, etc.), and the acoustic properties of the particle and fluid (size, shape, and density of the particle, viscosity and density of the fluid, etc.). Numerous researchers have dedicated their efforts to optimizing acoustofluidic devices and studying the underlying mechanisms of particle manipulation. Nama *et al.*[9] introduced impedance boundary conditions to represent channel walls based on a two-dimensional (2D) cross-sectional model established by Muller *et al.*[18] Their work

discussed the influences of the wall impedance, particle size, and phase difference between SAWs on the SSAW fields. Building on this simplified 2D model, extensive numerical and experimental studies have been conducted to investigate the influences of critical parameters on SSAW-based acoustophoresis. Devendran *et al.*[19] revealed that the pressure distribution and streaming field exhibit a degree of variation along the channel width due to the presence of a traveling wave component when two opposite-traveling and gradually decaying SAWs are superimposed. They observed larger traveling wave components and stronger streaming vortices near the side walls. Expanding on the findings of the lateral spatial dependence of the dominant force, Devendran *et al.*[20] further investigated the effects of channel height on the streaming field, and the optimum heights were quantified, which leads to the occurrence of the weakest streaming. Sachs *et al.*[21] studied the channel height dependence of the streaming pattern and the critical particle size for switching between the radiation-force-dominance regime and viscous-force-dominance regime. In addition to using the streaming effects and particle size sensitivity as performance metrics for particle aggregation, Dong *et al.*[22] determined the optimum range of heights based on the highest accuracy of particle aggregation. Apart from the studies focusing on the geometry of the microchannel, Wang *et al.*[23] investigated the resultant pressure distribution and particle trajectories with different configurations of the acoustofluidic device. Regarding the placement of IDTs, Wu *et al.*[24] developed a novel tilt-angle configuration of IDTs, where SSAW is at a certain angle relative to the continuous flow. This configuration of IDTs enhanced the separation efficiency by 32% with same power consumption.

Furthermore, to the previous studies of simplified 2D models, Hsu and Chao[25] demonstrated a full-wave model that considers the elastodynamics of the solid walls and the electromechanics of the piezoelectric substrate to investigate the effects of dimensions and locations of the channel on acoustophoresis. They found that the critical particle size could be reduced by an order of magnitude by adjusting the channel location. To enable a better knowledge of acoustophoresis, Liu *et al.*[26] recently developed a novel three-dimensional (3D) microfluidic model that simplifies the modeling of the substrate and microchannels, which are used to study the effects of the tilt angle of IDTs, SAW frequency, and flow rate on the manipulation of particles. Progressing from the simplified 3D model, Liu *et al.*[27] established a fully coupled 3D model for SSAW-based microfluidic device and simulated the particle trajectories with different particle radii. Das and Bhethanabotla[28] developed a thermo-pressure acoustic model and applied it to the modeling of 3D thermoviscous acoustofluidic systems. Thanks to the development of feasible 3D numerical simulations, Marefati *et al.*[17] investigated the influences of crucial parameters on acoustic streaming and particle concentration.

In this work, the governing equations are solved using the perturbation method and the finite element method (FEM) to numerically obtain the resultant fluid field and particle trajectory. This study aims to explore the influences of the microchannel height on the distribution and magnitude of the SSAW-induced physical fields, the timescale of particle aggregation, and the size- and space-dependent particle aggregation patterns. Our previous work[22] adopted the conventional freeze-wall boundary condition for simulating particle trajectory. In the current study, it has been replaced by the bounce-wall boundary condition, resulting in a better prediction of particle motions after striking the solid wall. This boundary condition allows the majority of the particles to be aggregated at PNs, so a more appropriate indicator, i.e., aggregation time instead of aggregation accuracy, can be used to better describe the performance of the device. In addition, we have extended our investigation to a much broader range of channel heights and discussed the propagation mechanism of the ultrasonic wave along the height-wise direction. These improvements enable us to propose, for the first time, a generic formula for the optimal channel height. Furthermore, while the critical particle size has been widely studied, its dependence on the channel height and the phenomenon of localized aggregation remains unclear. Hence, our study also fills this gap. The findings gain insights into the design of SSAW-based microfluidic devices.

II. MATHEMATICAL MODEL

A. Governing equations of the fluid

In the fluid domain, the continuity equation and Navier–Stokes equation for a viscous compressible fluid are derived by the conservation of mass and momentum[29–31]

$$\frac{\partial \rho}{\partial t} + \nabla \cdot (\rho \boldsymbol{v}) = 0, \tag{1}$$

$$\rho \frac{\partial \boldsymbol{v}}{\partial t} + \rho(\boldsymbol{v} \cdot \nabla)\boldsymbol{v} = -\nabla p + \mu \nabla^2 \boldsymbol{v} + \left(\mu_b + \frac{\mu}{3}\right)\nabla(\nabla \cdot \boldsymbol{v}), \tag{2}$$

where ρ, $\boldsymbol{v}$, p, μ, and μ_b are the mass density, fluid velocity, fluid pressure, shear viscosity, and bulk viscosity, respectively. To solve Eqs. (1) and (2), the thermodynamic equation of state is introduced as a constitutive equation, in which pressure p is expressed as a function of density ρ with the assumption of constant entropy in time and space[32]

$$p_1 = c_0^2 \rho_1, \tag{3}$$

where c_0 is the isentropic speed of sound in the liquid.

A challenge of solving these non-linear governing equations lies in the different characteristic time scales between the imposed periodic acoustic oscillations with frequency of 1–100 MHz and the non-linear streaming and particle movement with characteristic time of tenth of second to several minutes.[9,25] The introduction of ultrasonic waves to the fluid induces small perturbations to the acoustofluidic fields, which can be expressed by the summation of a quiescent component, a time-harmonic component (fluid response to the periodic acoustic excitation), and a steady component (time-averaged acoustic streaming over an oscillation period)

$$\boldsymbol{v} = \boldsymbol{v}_0 + \boldsymbol{v}_1 + \boldsymbol{v}_2 + O(\epsilon^3) + \cdots, \tag{4a}$$

$$p = p_0 + p_1 + p_2 + O(\epsilon^3) + \cdots, \tag{4b}$$

$$\rho = \rho_0 + \rho_1 + \rho_2 + O(\epsilon^3) + \cdots, \tag{4c}$$

where ϵ is a non-dimensional small parameter ($\ll 1$). The subscript 0 refers to the quiescent component, which is independent of the actuation of acoustic waves, 1 refers to the first-order component, and 2 refers to the second-order component. The contributions from the terms higher than second order are relatively small and negligible. The first-order and second-order equations can be obtained by grouping terms in the governing equations according to ϵ.

Substituting Eq. (4) into Eqs. (1) and (2) and collecting only the first-order terms, which contains ϵ, yields the first-order equations

$$\frac{\partial \rho_1}{\partial t} = -\rho_0 \nabla \cdot \boldsymbol{v}_1, \tag{5}$$

$$\rho_0 \frac{\partial \boldsymbol{v}_1}{\partial t} = -\nabla p_1 + \mu \nabla^2 \boldsymbol{v}_1 + \left(\mu_b + \frac{\mu}{3}\right) \nabla(\nabla \cdot \boldsymbol{v}_1). \tag{6}$$

To simplify the mathematical processes, we assume a time harmonic dependence of all the first-order terms by adding a complex expression $e^{i\omega t}$,

$$\boldsymbol{v}_1(\boldsymbol{x}, t) = \boldsymbol{v}_1(\boldsymbol{x}) e^{i\omega t}, \tag{7a}$$

$$p_1(\boldsymbol{x}, t) = p_1(\boldsymbol{x}) e^{i\omega t}, \tag{7b}$$

$$\rho_1(\boldsymbol{x}, t) = \rho_1(\boldsymbol{x}) e^{i\omega t}, \tag{7c}$$

where $\boldsymbol{x}$ is the position vector; $\boldsymbol{v}_1(\boldsymbol{x})$, $p_1(\boldsymbol{x})$, and $\rho_1(\boldsymbol{x})$ are the time-independent complex fields in space. i is the imaginary unit, $\omega = 2\pi f$ is the angular frequency, and f is the frequency of the imposed acoustic field. By inserting Eq. (7) into Eqs. (5) and (6), every time derivative $\partial/\partial t$ can be replaced by multiplying by a factor of $i\omega$, yielding

$$i\omega \rho_1 = -\rho_0 \nabla \cdot \boldsymbol{v}_1, \tag{8}$$

$$i\omega \rho_0 \boldsymbol{v}_1 = -\nabla p_1 + \mu \nabla^2 \boldsymbol{v}_1 + \left(\mu_b + \frac{\mu}{3}\right) \nabla(\nabla \cdot \boldsymbol{v}_1), \tag{9}$$

where the solution to the original real-number governing equations can be obtained by taking the real part of the complex field solved from Eqs. (8) and (9) [e.g., $\boldsymbol{v}_1 = \mathrm{Re}[\boldsymbol{v}_1 e^{i\omega t}]$, where $\boldsymbol{v}_1$ on the left side is the desired physical field, while the $\boldsymbol{v}_1$ within the bracket is the complex field solved from Eqs. (8) and (9)].

The second-order terms cause the stationary acoustic streaming, which cannot be produced by pure sinusoidal variation. Due to the significant timescale discrepancy between the acoustic vibration and acoustic streaming, the second-order effects are averaged over a period of oscillation T, denoted by $\langle X \rangle \equiv \frac{1}{T}\int_0^T X(t)dt$, yielding the time-averaged second-order equations

$$-\nabla \cdot \langle \rho_1 \cdot \boldsymbol{v}_1 \rangle = \rho_0 \nabla \cdot \langle \boldsymbol{v}_2 \rangle, \tag{10}$$

$$\left\langle \rho_1 \frac{\partial \boldsymbol{v}_1}{\partial t} \right\rangle + \rho_0 \langle (\boldsymbol{v}_1 \cdot \nabla) \boldsymbol{v}_1 \rangle = -\nabla \cdot \langle p_2 \rangle + \mu \nabla^2 \langle \boldsymbol{v}_2 \rangle + \left(\mu_b + \frac{\mu}{3}\right) \nabla(\nabla \cdot \langle \boldsymbol{v}_2 \rangle), \tag{11}$$

where transient processes are neglected, and the time-averaged values of the first-order terms and $\left\langle \frac{\partial \boldsymbol{v}_2}{\partial t} \right\rangle$ are zero. The non-zero velocity $\langle \boldsymbol{v}_2 \rangle$ is the acoustic streaming velocity, which is generated due to the absorption of energy and momentum from the imposed acoustic waves. The non-zero pressure $\langle p_2 \rangle$ generates the radiation force that arises from the scattering of acoustic waves.

B. Acoustophoretic forces on single microparticles

In practical biological applications, buoyancy and gravity forces are nearly balanced out, leaving only acoustic radiation force and viscous force (i.e., Stokes drag force) to control the particle motion. Assuming neutral-buoyance particles with sizes much smaller than the acoustic wavelength in a dilute-suspension case, we can neglect particle–particle interaction and particle-induced fluid motion. The radiation force, induced by the scattering of the sound wave, is the main force driving the acoustophoretic phenomena, while the Stokes drag force, exerted by the second-order acoustic streaming, can hamper particle accumulation. Although the second-order effects are responsible for the acoustic radiation force, for spherical particles with radii r much smaller than the acoustic wavelength ($r \ll \lambda_{SAW}$, i.e., particle radii within the range of 0.1 to 10 μm in the context of our study), we can obtain the time-averaged radiation force based solely on the first-order quantities, as follows:[33,34]

$$\boldsymbol{F}_{\mathbf{rad}} = -\pi r^3 \left[\frac{2\kappa_0}{3} \mathrm{Re}\left[f_1^* p_1^* \nabla p_1\right] - \rho_0 \mathrm{Re}\left[f_2^* \boldsymbol{v}_1^* \nabla \boldsymbol{v}_1\right]\right], \tag{12a}$$

where κ_0 is the compressibility of the fluid and the asterisk represents the complex conjugate. The monopole scattering coefficient f_1 and dipole scattering coefficient f_2 are expressed as

$$f_1 = 1 - \frac{\kappa_p}{\kappa_0}, \tag{12b}$$

$$f_2 = \frac{2(1-\gamma)(\rho_p - \rho_0)}{2\rho_p + \rho_0(1-3\gamma)}, \tag{12c}$$

$$\gamma = -\frac{3}{2}\left[1 + i\left(1 + \frac{\delta}{a}\right)\right]\frac{\delta}{a},\ \delta = \sqrt{\frac{2\mu}{\omega\rho_0}}, \tag{12d}$$

where ρ_p, δ, and γ are the density of the particle, thickness of the viscous boundary layer, and δ-dependent variable, respectively. The compressibility of the fluid κ_0 and the compressibility of the particle κ_p are defined as[34,35]

$$\kappa_0 = \frac{1}{\rho_0 c_0^2}, \tag{13}$$

$$\kappa_p = \frac{3(1-\sigma_p)}{1+\sigma_p}\frac{1}{\rho_p c_p^2}, \tag{14}$$

where σ_p and c_p are the Poisson's ratio of the solid particle and the speed of sound of the particle, respectively. The streaming-induced Stokes drag force is determined by the relative velocity between the particle velocity $\boldsymbol{v}_p$ and the second-order streaming velocity $\langle \boldsymbol{v}_2 \rangle$, as follows:

$$\boldsymbol{F}_{\mathbf{drag}} = 6\pi\mu r\,(\langle \boldsymbol{v}_2 \rangle - \boldsymbol{v}_p). \tag{15}$$

The Stokes drag force can be determined by using the solutions to the second-order equations.

Once the solution to the radiation force and the Stokes drag force is known, the particle trajectory can be determined based on Newton's second law of motion

$$m_p \frac{\mathrm{d}(\boldsymbol{v}_p)}{\mathrm{d}t} = \boldsymbol{F}_{\mathbf{drag}} + \boldsymbol{F}_{\mathbf{rad}}, \tag{16}$$

where m_p is the mass of the particle. The inertia of the particle can be ignored because the timescale of the acceleration is relatively small compared to the total duration of particle motions.[31] By setting the left side of Eq. (16) to zero and substituting Eq. (15) into Eq. (16), the particle velocity can be expressed as

$$\boldsymbol{v}_p = \langle \boldsymbol{v}_2 \rangle + \frac{\boldsymbol{F}_{\mathbf{rad}}}{6\pi\mu r}. \tag{17}$$

By solving Eq. (17), the particle trajectories can be predicted.

C. Acoustic energy

To facilitate the analyses of results from the energy perspective, we hereby introduce the time-averaged total acoustic energy density E_{tot} for the first-order fluid response and the kinetic energy density e_{kin} for the second-order fluid response, which are defined as[21,36]

$$E_{tot} = \frac{1}{2}\kappa_0\langle p_1 p_1^*\rangle + \frac{1}{2}\rho_0\langle \boldsymbol{v}_1 \boldsymbol{v}_1^*\rangle, \tag{18}$$

$$e_{kin} = \frac{1}{2}\rho_0 \boldsymbol{v}_2{}^2, \tag{19}$$

where the total acoustic energy density E_{tot} consists of the potential energy density $E_{pot} = \frac{1}{2}\kappa_0\langle p_1 p_1^*\rangle$ and the kinetic energy density $E_{kin} = \frac{1}{2}\rho_0\langle \boldsymbol{v}_1 \boldsymbol{v}_1^*\rangle$.

III. NUMERICAL MODEL

A. Model configuration and physical description

A 3D sketch of a typical SSAW-based device for particle aggregation is demonstrated in Fig. 1. The device consists of a Y-cut lithium niobate ($LiNbO_3$) piezoelectric substrate, onto which a pair of metallic interdigital transducers (IDTs) with a periodic electrode configuration is bonded. The microchannel, located between the IDTs, is filled with water and made of a bio-compatible soft elastic poly-dimethylsiloxane (PDMS) material (Sylgard-184-silicone elastomer base and Sylgard-184-silicone elastomer curing agent mixed at a ratio of 10:1 by weight[37]). When hormonic electric signals are applied to the IDTs, two counter-propagating traveling SAWs (TSAW) are generated at the surface of the substrate, resulting in the formation of SSAW. Following the Huygens–Fresnel principle,[38,39] the SAWs leak upwards into the fluid domain at a Rayleigh angle, forming an oscillatory pressure distribution and actuating the acoustic streaming inside the overlying microchannel.

Figure 2 illustrates the underlying physics of the formation of SSAW and the related phenomena in the cross-sectional view. The TSAW that propagates on the surface of the substrate is the so-called Rayleigh wave, and its amplitude decays exponentially toward the substrate to a depth of 1–2 wavelengths. Therefore, most of the energy is constrained to the surface of the substrate.[9,10] The displacement of the TSAW has 90° phase difference in time in different directions (x and z directions), leading to the elliptical displacement. The TSAWs propagate along PDMS–substrate interface and fluid–substrate interface and leak energy directly into the PDMS and fluid with a refraction angle θ, as denoted by the blue and red arrows in Fig. 2. The refraction angle is defined as the ratio of the speed of sound in the two different media[10]

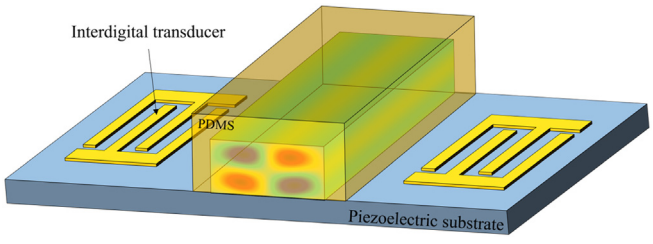

FIG. 1. Three-dimensional sketch of the SSAW-based device consisting of the PDMS microchannel filled with water and two interdigitated transducers bonded on the piezoelectric substrate.

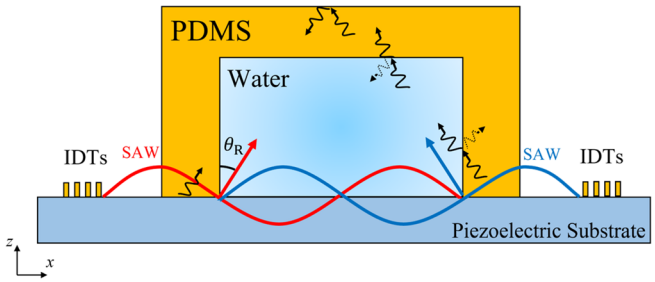

FIG. 2. Illustration of SAW propagation in cross-sectional view.

$$\theta = \frac{c_{mat}}{c_{sub}}, \tag{20}$$

where c_{mat} and c_{sub} are the speed of sound of the refracted material and vibrating substrate, respectively. Hence, $\theta_{PDMS-sub} = c_{PDMS}/c_{sub}$ at PDMS–substrate interface, where c_{PDMS} is the speed of sound in PDMS; $\theta_{f-sub} = c_0/c_{sub}$ at fluid–substrate interface. In the transverse direction of the channel, two TSAWs travel toward each other and decay exponentially along their paths, forming SSAW with traveling wave components.[19] The mismatch of the amplitudes of the two counter-propagating TSAWs causes the traveling wave components, which are particularly obvious near the two side edges of the channel when the channel width is relatively large.

Apart from the direct leakage of TSAWs from the surface of the vibrating substrate, TSAWs also leak into the fluid through several other indirect ways, including transmission and reflection at the PDMS–air and fluid–PDMS interfaces, as indicated by the black arrows in Fig. 2. Waves that leak into the PDMS wall are reflected at the PDMS–air interface and travel back to the fluid through the PDMS–fluid interface. While the wave reflection coefficient from PDMS to air is nearly equal to one, indicating that the majority of the incident waves toward the PDMS–air interface will be reflected back to the PDMS, the damping coefficient for PDMS walls thicker than 2 mm and wave frequencies larger than 6 MHz is large enough to assume all the waves propagating through the PDMS wall are absorbed.[9,31] Therefore, we neglect the waves reflected at the PDMS–air interface and only consider reflections at the fluid–PDMS interface. The pseudo-standing waves are formed in the vertical direction by the superposition of upward-propagating waves emitted from the substrate–fluid interface and the weaker waves reflected at the fluid–PDMS interface with a small yet non-zero reflection coefficient. The pseudo-standing wave can also be understood as the combination of a standing wave and a traveling wave.

Given that the primary flow is uniform along a long and straight channel, we can disregard any changes caused by the imposed acoustic waves in the streamwise direction (y direction). Because of the high computational cost required by an intricate 3D model, a 2D cross-sectional model over the x–z plane has been established, as shown in Fig. 3. Appropriate conditions (as discussed in Sec. III B) are imposed on boundaries Γ_i and Γ_v of the computational domain Ω to represent the characteristics of the surrounding PDMS walls and acoustic excitation on the substrate. The 2D model has been proved to simulate the resultant physical fields with sufficient accuracy as long as the thickness of the PDMS wall is larger than the PDMS damp length,[40] which

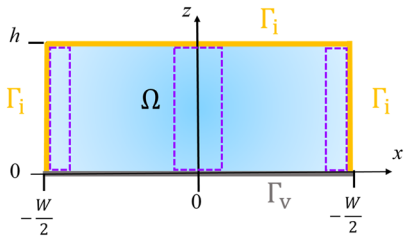

FIG. 3. Computational model of the SSAW-based device in cross-sectional view.

is the case in our study. In addition, the established 2D model can effectively capture the essence of particle aggregation process, as the acoustic waves primarily influence the particle movement in the transverse and vertical directions. In contrast, the longitudinal movement of particles is mainly governed by the discharge rate of the particle–fluid mixture within the microchannel. Due to the nature of aggregating particles at PNs (in the middle and beside two sidewalls of the channel in our case), three target boxes are configured at the center of PNs to count the number of aggregated particles, as shown by the dotted purple rectangles in Fig. 3.

In order to actuate the system at the full-wave resonance at the bottom, the actuation frequency f is chosen to be 6.65 MHz and the width of the microchannel is $W = \lambda_{SAW} = c_{sub}/f = 600\ \mu$m. The displacement amplitude of the acoustic wave is $u_0 = 0.1$ nm. Our case is considered isothermal, so the temperature is fixed at $T = 25\,^{\circ}$C. The key parameters of water are its density of undisturbed water $\rho_0 = 997\,\mathrm{kg/m^3}$, speed of sound $c_0 = 1497\,\mathrm{m/s}$, bulk viscosity $\eta_b = 2.47\,\mathrm{mPa\,s}$, shear viscosity $\eta = 0.89\,\mathrm{mPa\,s}$, and compressibility $\kappa_0 = 448\,\mathrm{TPa^{-1}}$; the key properties of polystyrene are its density $\rho_p = 1050\,\mathrm{kg/m^3}$, speed of sound $c_p = 2350\,\mathrm{m/s}$, and compressibility $\kappa_p = 249\,\mathrm{TPa^{-1}}$; the key properties of PDMS are density $\rho_{PDMS} = 920\,\mathrm{kg/m^3}$ and speed of sound $c_{PDMS} = 1076.5\,\mathrm{m/s}$, while the key properties of $LiNbO_3$ are density $\rho_{sub} = 4648\,\mathrm{kg/m^3}$ and speed of sound $c_{sub} = 3994\,\mathrm{m/s}$.[18,35,41–45]

B. Boundary conditions

The impedance boundary condition is applied to the soft PDMS channel walls to mimic the behavior of PDMS material, as depicted by the impedance boundaries Γ_i in Fig. 3. The impedance boundary condition on Γ_i is governed by the following equations:[9,46]

$$\boldsymbol{n}\cdot\nabla p_1 = \mathrm{i}\frac{\omega\rho_0}{Z_{PDMS}}p_1,\ \text{on}\ \Gamma_i, \tag{21a}$$

$$Z_{PDMS} = \rho_{PDMS}\times c_{PDMS}, \tag{21b}$$

where Z_{PDMS} represents the acoustic impedance of the PDMS channel wall. The impedance boundary condition assumes that all traveling waves in the thick PDMS walls are absorbed. In the case of silicon or glass walls, the hard-wall boundary condition, $\boldsymbol{n}\cdot v_1 = 0$, is utilized.

The boundary condition at the piezoelectric substrate is represented by the displacement functions in the transverse and vertical directions (x and z directions). The displacement function of a traveling Rayleigh wave on the piezoelectric substrate can be described as follows:[32,47]

$$u_x(x,t) = \gamma u_0 e^{-C_d x}e^{i\omega t}, \tag{22a}$$

$$u_z(x,t) = -u_0 e^{-C_d x}e^{i\omega t}, \tag{22b}$$

where $k = 2\pi/\lambda$ is the wavenumber, u_0 is the displacement amplitude in the z direction, γ is the ratio of displacement amplitude in the x and z directions, and C_d is the SAW decay coefficient defined by[48]

$$C_d = \frac{\rho_0 c_0}{\rho_{sub}c_{sub}\lambda_{SAW}}. \tag{23}$$

For the actuation frequency of 6.65 MHz, the value of C_d is $116\,\mathrm{m^{-1}}$.[9] The displacement of the SSAW is derived based on Eq. (22)

$$u_x(x,t) = \gamma u_0\left[e^{-C_d\left(\frac{W}{2}-x\right)}e^{i\left[-k\left(\frac{W}{2}-x\right)+\omega t\right]} + e^{-C_d\left(\frac{W}{2}+x\right)}e^{i\left[-k\left(\frac{W}{2}+x\right)+\omega t\right]}\right], \tag{24a}$$

$$u_z(x,t) = -u_0\left[e^{-C_d\left(\frac{W}{2}-x\right)}e^{i\left[-k\left(\frac{W}{2}-x\right)+\omega t-\frac{\pi}{2}\right]} - e^{-C_d\left(\frac{W}{2}+x\right)}e^{i\left[-k\left(\frac{W}{2}+x\right)+\omega t-\frac{\pi}{2}\right]}\right], \tag{24b}$$

where the $\pi/2$ phase shift between the two counter-propagating TSAWs is denoted by the subtraction of $\pi/2$ in the z direction, and the elliptical displacement of SAW is presented by the different signs of the z-component displacements of the two counter-propagating SAWs. To enable the specification of velocity boundary condition in the FEM analysis, the displacement function in Eq. (24) is differentiated with respect to time to obtain the velocity profile. The time-dependent terms are then removed from the velocity equations to enable the frequency domain analysis, leading to the following velocity boundary condition on Γ_v,

$$v_x(x,t) = \gamma u_0\omega\left[e^{-C_d\left(\frac{W}{2}-x\right)}e^{i\left[-k\left(\frac{W}{2}-x\right)\right]} + e^{-C_d\left(\frac{W}{2}+x\right)}e^{i\left[-k\left(\frac{W}{2}+x\right)\right]}\right], \tag{25a}$$

$$v_z(x,t) = -u_0\omega\left[e^{-C_d\left(\frac{W}{2}-x\right)}e^{i\left[-k\left(\frac{W}{2}-x\right)-\frac{\pi}{2}\right]} - e^{-C_d\left(\frac{W}{2}+x\right)}e^{i\left[-k\left(\frac{W}{2}+x\right)-\frac{\pi}{2}\right]}\right]. \tag{25b}$$

The oscillations in the x direction can be disregarded since only the vertical oscillation induces the pressure distribution in the fluid. Furthermore, the decay along the paths can also be neglected due to the small width of the channel.

For the second-order terms, the Dirichlet no-slip boundary condition is imposed on all boundaries (Γ_V and Γ_I)

$$\boldsymbol{v}_2 = 0\ \text{on}\ \Gamma_V\quad\text{and}\quad\Gamma_I. \tag{26}$$

It is worth mentioning that strictly speaking the solid boundaries are not static. However, as the difference between the initial and deformed positions is relatively small, we can neglect the boundary movement and apply the no-slip boundary condition to all boundary positions.

In simulating particle trajectories, the particle–wall interactions at four boundaries are usually represented by the freeze-wall boundary condition in the previous numerical studies,[9,22] which set the particle velocity to zero and fix the particle position at the time of impact. In practice, a particle in contact with a solid wall will not be stuck at the contact point and lose its momentum; instead, it will be reflected from the wall. This discrepancy leads to the inaccurate particle trajectory and poor representation of particle manipulation. We hereby employ the bounce-wall boundary condition [$\boldsymbol{v}_p = \boldsymbol{v}_c - 2(\boldsymbol{n}\cdot\boldsymbol{v}_c)\boldsymbol{n}$, where $\boldsymbol{v}_c$ is the particle velocity when striking the wall], treating the walls as perfectly reflective boundaries. Figure 4 demonstrate the discrepancy

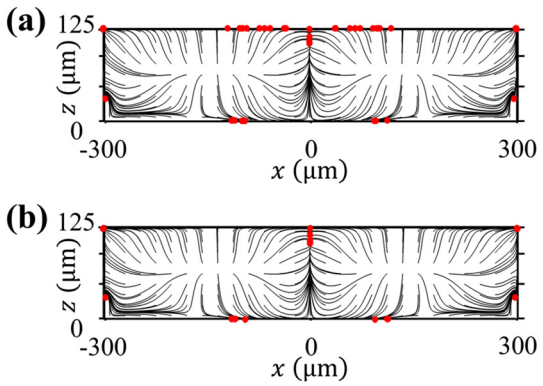

FIG. 4. Comparison of the final positions of 10 μm particles under different boundary conditions. (a) Freeze-wall boundary condition. (b) Bounce-wall boundary condition.

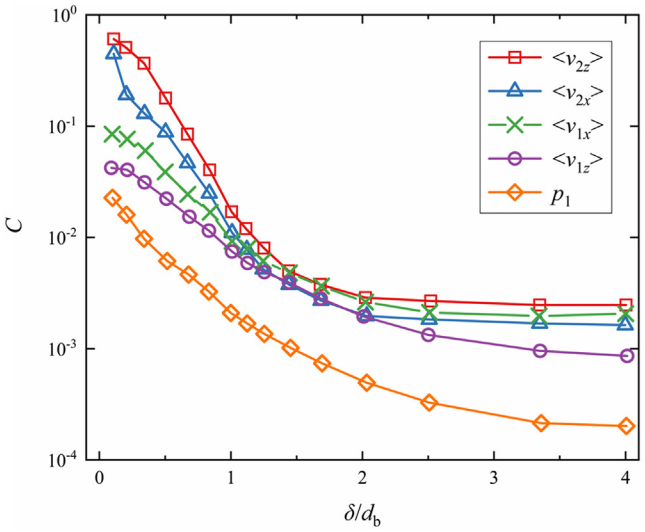

FIG. 5. Mesh convergence analysis: the relative convergence parameter C for different physical fields as a function of the meshing parameter δ/d_b.

under different boundary conditions. We can observe that a few particles are eventually stuck at the upper and lower boundaries with the freeze-wall boundary condition, which is unlikely to happen in laboratory observation. In contrast, when using the bounce-wall boundary condition, nearly all particles move toward PNs driven by the radiation force. Although several particles near the bottom wall are trapped in both cases, close scrutinization shows that they actually undergo different motions. Particles in Fig. 4(a) are stuck at the bottom wall with zero velocity, while particles in Fig. 4(b) are circulating within the regions dominated by streaming force.

C. Numerical validation and implementation

Following our previous work,[22] the FEM is employed to discretize the differential equations in space and time, allowing for a numerical solution to be obtained. Mesh convergence analysis is conducted by examining the relative convergence parameter $C(g) = \sqrt{\int (g - g_{\text{ref}})^2 \mathrm{d}x\mathrm{d}z / \int (g_{\text{ref}})^2 \mathrm{d}x\mathrm{d}z}$ for a numerical solution g with respect to a reference solution g_{ref} resulting from the finest mesh $d_b = 0.2\delta$, as shown in Fig. 5. To fully capture the flow in the thin boundary layers near the solid–fluid interfaces, we set the maximum element size near the boundary to be $d_{\text{layer}} = 0.3\delta$, and the maximum element size in the middle of the fluid domain to be $d_b = 10d_{\text{layer}}$, which has been shown to give sufficient resolution according to our mesh convergence analysis.

Furthermore, the numerical implementation of our model has been verified against both numerical and experimental results from Mao *et al.*[49] Corresponding to their work, the rectangular PDMS channel encloses the water domain with a width of 170 μm and a height of 60 μm, and the SAW is applied at a frequency of 12.883 MHz with a wavelength of 300 μm. To maintain consistency with their work for comparison, the particle–wall interactions are initially represented by the freeze-wall boundary condition. Figure 6 shows a comparison between the results reported in Mao *et al.*[49] and those obtained from our simulation. Figures 6(a)–6(c), 6(g), and 6(h) present the results when PN is located at the center of the channel, while Figs. 6(d)–6(f), 6(i), and 6(j) display the results when AN is located at the center of the channel. Figures 6(a), 6(d), 6(g), and 6(i) demonstrate the radiation force potential with radiation force vectors represented by black arrows, pointing from the regions of maximum radiation force potential (red) to the regions of minimum radiation force potential (blue). The computed trajectories (blue lines) and final positions (red points) of the 5.022 μm polystyrene beads are shown in Figs. 6(b), 6(e), 6(h), and 6(j). The experimental traces of particles move along three lines in the middle and near two sidewalls for the case of PN at the center, while particle trajectories only leave two traces near the two sidewalls for the case of AN at the center. In Figs. 6(e) and 6(j), it is noted that several particles are stuck at the bottom away from the two sidewalls, which slightly differs from the experimental results. These discrepancies can be attributed to the idealized assumptions in the numerical model, such as uniform flow velocity, homogeneous particle distribution, and negligible particle–particle interaction. Furthermore, it can be attributed to the freeze-wall boundary condition applied in simulating the particle trajectories. Under such a boundary condition, particles will lose their momentum once they touch the wall. Under the bounce-wall boundary condition, near-bottom particles tend to slide closer toward the two sidewalls with a distance of less than 10 μm, as shown in Fig. 6(k). When switching to the bounce-wall boundary condition, our numerical results show better agreement with the experimental observations than Mao *et al.*[49]

IV. PARAMETRIC STUDIES CONCERNING CHANNEL HEIGHT

A. Influences on physical fields

Physical fields induced by the SSAW potentially play important roles in the performance of acoustophoresis. The acoustofluidic fields consist of the acoustic wave field indicated by the first-order quantities and the corresponding fluid field indicated by the second-order quantities. They induce the force fields that directly drive particle motion. In addition, energy fields are also considered below to enrich the

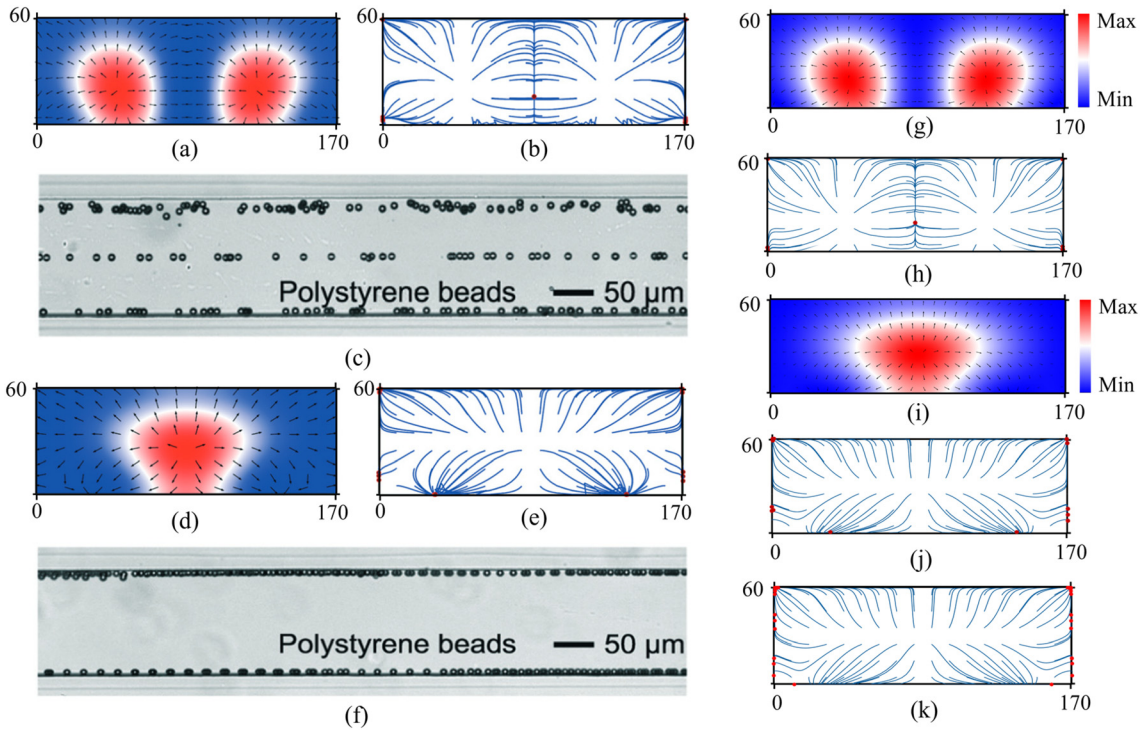

FIG. 6. Comparison of the radiation force potential fields, radiation force fields, and numerical and experimental trajectories of 5.022 μm polystyrene beads between (a)–(f) Mao *et al.*'s results[49] and (g)–(k) our simulation results. (a), (d), (g), and (i) Acoustic radiation force and its potential fields in the *x*–*z* plane view. (b), (e), (h), and (j) Numerical trajectories and final positions of the polystyrene beads in the *x*–*z* plane view under freeze-wall boundary condition. (k) Numerical trajectories under bounce-wall boundary condition. (c) and (f) Experimental traces of the polystyrene beads in the *y*–*x* plane view.

analyses. To gain insight into the underlying physics of these fields in a closed rectangular microchannel cross section, we carry out a series of numerical simulations, where we vary the channel heights from 40 to 960 μm, while maintaining a constant the channel width.

1. Spatial distribution

In Fig. 7, we demonstrate the spatial distribution of acoustofluidic fields, including the first-order acoustic pressure p_1, the first-order acoustic velocity $\boldsymbol{v}_1$, and the time-averaged second-order velocity $\langle \boldsymbol{v}_2 \rangle$,

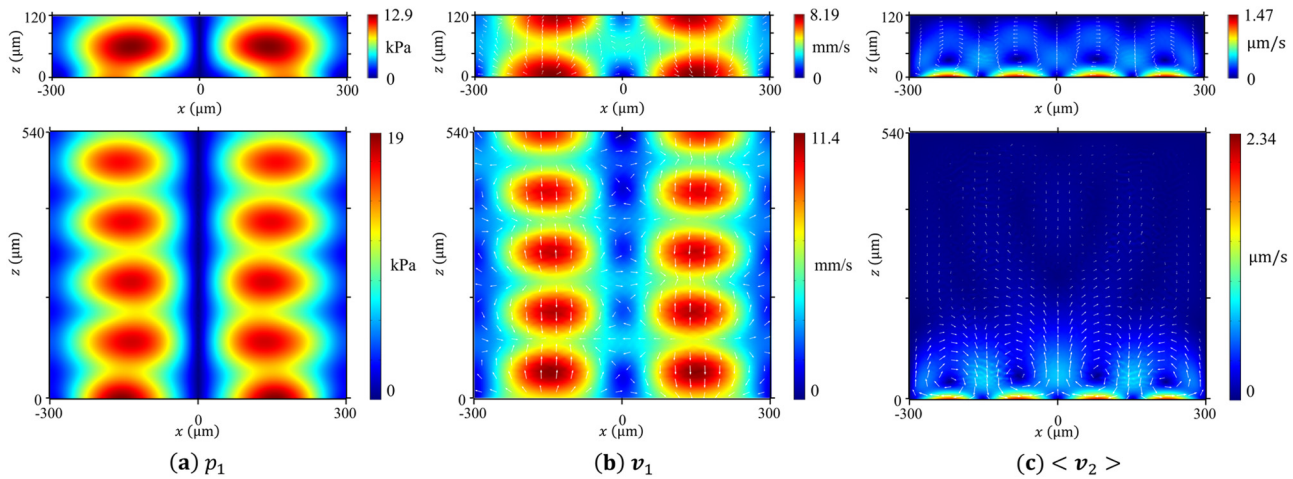

FIG. 7. Acoustofluidic fields at channel heights of $h = 120$ μm and $h = 540$ μm: (a) first-order pressure field, (b) first-order velocity field, and (c) time-averaged second-order velocity field.

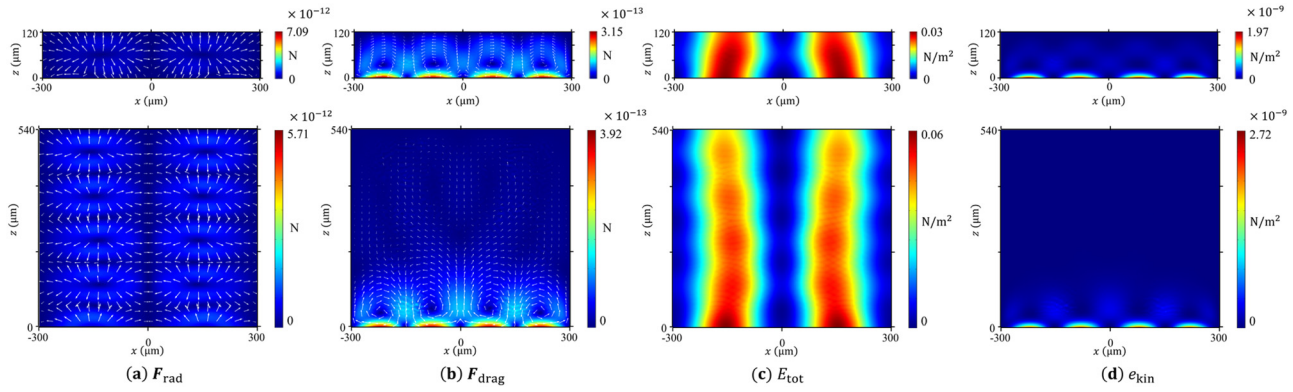

FIG. 8. Force fields and energy fields at channel heights of $h = 120$ and $540\ \mu$m: (a) radiation force field, (b) Stokes drag force field, (c) total acoustic energy density of the first-order field, and (d) kinetic energy density of the second-order field. Force and energy magnitude is shown as colors ranging from zero (blue) to maximum value (red), while vectors are denoted as white arrows.

at two representative channel heights $h = 120$ and $540\ \mu$m. The magnitude of these parameters is displayed using colourmaps ranging from maximum (red) to minimum (blue) values, and vectors are shown as white arrows. In Figs. 7(a) and 7(b), three PNs can be observed in the horizontal direction due to the superposition of two counter-propagating TSAWs at the surface of the substrate. Meanwhile, the first-order acoustofluidic fields exhibit a periodic distribution in the vertical direction, indicating the oscillatory propagation of the leaky traveling waves from the bottom toward the top. As the pseudo-standing wave in the vertical direction is formed by the reflection at the upper PDMS wall (i.e., from low-impedance material to high-impedance material), the resultant pressure nodal position of this pseudo-standing wave is captured at the top of the channel $z = h$. With the change of the channel height, the pressure antinodes immediately above the channel bottom shift up and down periodically from $z = 0$ to $60\ \mu$m (e.g., AN at $z = 60\ \mu$m for $h = 120\ \mu$m but at $z = 0\ \mu$m for $h = 540\ \mu$m), as waves travel different distance until being reflected at the top. In contrast, the second-order velocity field is actuated by the attenuation of the leaky waves from the bottom boundary and is confined in the near-bottom region of the channel ($z < \lambda_{SAW}/4 = 150\ \mu$m, as the vertical extension of acoustic streaming equals the horizontal one[18]) where four streaming vortices can be observed in Fig. 7(c). Owing to the nature of the bottom-driven system (i.e., SAW excitation only at the bottom interface), the magnitude of streaming becomes much weaker in the upper region of the channel ($z > 150\ \mu$m), and the spatial distribution of $\langle \boldsymbol{v}_2 \rangle$ does not change significantly with the increase in the channel height. When the channel height is relatively large (e.g., $h = 540\ \mu$m), two blurry streaming vortices can be observed in the upper region, which is the secondary effects induced by the four vortices near the bottom.

The force fields and energy fields are derived from the acoustofluidic fields, as discussed in Sec. II. From Eqs. (15) and (19), the Stokes drag force $\boldsymbol{F}_{drag}$ and the kinetic energy density of the second-order field e_{kin} are proportional to $\boldsymbol{v}_2$ and $\boldsymbol{v}_2{}^2$, respectively. Therefore, their spatial distributions in Figs. 8(b) and 8(d) are akin to the distribution of the second-order velocities in Fig. 7(c), where they are all constrained near the substrate. In relation to the first-order fields, the radiation force $\boldsymbol{F}_{rad}$ presents a periodic distribution with vectors denoted by the white arrows always pointing away from the antinodes, and the total acoustic energy density of the first-order fields E_{tot} reveals a column-shape distribution with the higher energy zone at antinodes (red) and the lower energy zone at nodes (blue), as shown in Figs. 8(a) and 8(c). Resulting from the periodic variation of the first-order pressure nodal positions in the vertical direction, the cellular structure of the radiation force field emerges periodically from the bottom wall in Fig. 8(a).

2. Vertical periodicity of wave interference pattern

The periodicity of the first-order pressure field in the vertical direction is further investigated. Recent work noted that the interactions between a TSAW and a microchannel can induce microscale interference patterns.[50] A substrate-bound TSAW produces a wavefront that propagates at $c_{sub} = \lambda_{SAW} f$ along the bottom wall, and we term it as the "SAW wavefront" as it has the same wavelength as the underlying SAW on the surface of the substrate. Based on the Huygens–Fresnel principle,[38] the channel wall serves as the source of the Huygens–Fresnel wavelets. Such wavelets will be generated as the SAW wavefronts propagate along the bottom, resulting in a wavefront that emanates from the bottom wall at a Rayleigh angle θ_R and travels at $c_0 = \lambda_f f$ within the fluid. Such wavefronts are termed as "fluid wavefronts." Figure 9 demonstrates that the combination of these

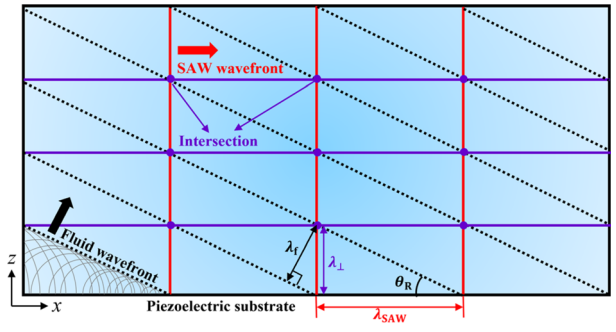

FIG. 9. Intersection of fluid wavefronts and SAW wavefronts yields pressure nodal positions parallel to the bottom channel wall for the case of a TSAW.

wavefronts produces the pressure nodal and antinodal positions parallel to the bottom wall. Where these wavefronts destructively interfere, minimum oscillation amplitude occurs. The vertical spacing of the repetitive interference pattern along the microchannel height $\lambda_\perp$ is obtained by trigonometry as shown in Fig. 9

$$\lambda_\perp = \lambda_{SAW} \tan\left(\sin^{-1}\frac{\lambda_f}{\lambda_{SAW}}\right) = 242\ \mu m. \tag{27}$$

The periodicity of the wavefront intersections $\lambda_\perp$ for the case of TSAW can also be applied to the case of SSAW, since the standing wave can be deemed as the superposition of two counter-propagating TSAWs. The resultant time-domain illustration of the propagation of SSAW can be found in the supplementary videos of Devendran *et al.*,[19] where the periodic variation of pressure nodal positions in the vertical direction can be observed. Through Eq. (27), we have established the relationship between $\lambda_\perp$ and λ_{SAW}. We hereby introduce a nondimensional parameter h/λ_{SAW}, which normalizes the channel height with λ_{SAW}.

3. Amplitude and spatial average

To gain a better understanding of the influences of channel height, we examine the overall strength of the acoustofluidic fields and force fields, as well as the spatial average of the energy fields, as a function of the non-dimensional parameter h/λ_{SAW} in Figs. 10–12. The maximum amplitude of acoustofluidic and force fields over the cross section are always captured at the first ANs immediately above the actuation boundary. The average total acoustic energy density $\bar{E}_{tot}$ of the first-order fields over the bulk of volume V and the average kinetic energy density $\bar{e}_{kin}$ of the second-order field over the cross section of area A can be derived from Eqs. (18) and (19), respectively,

$$\bar{E}_{tot} = \frac{1}{V}\int_V \left[\frac{1}{4}\kappa_0\left(p_1 p_1^*\right)^2 + \frac{1}{4}\rho_0\left(\boldsymbol{v}_1 \boldsymbol{v}_1^*\right)^2\right] dV, \tag{28}$$

$$\bar{e}_{kin} = \frac{\rho_0}{2hW}\int_A (u_2 + v_2)^2 dA, \tag{29}$$

where u_2 and v_2 are the x and y components of the second-order velocity $\boldsymbol{v}_2$. In Figs. 10–12, the amplitude and spatial average of these fields exhibit an oscillatory pattern with respect to the channel height, which results from the periodic variation of pressure nodal positions. The oscillation of the curve exhibits periodicity with a regular interval, as denoted by Δh_{max} in Fig. 10. Notably, all the physical fields undergo a slightly oscillatory decrement with the increase in the channel height, owing to the enhanced wave attenuation with increased vertical distance of travel. It is also worth noting that $\bar{e}_{kin}$ exhibits a more pronounced oscillatory decrease compared to $\bar{E}_{tot}$, due to the asymmetric nature of the second-order fields. In Fig. 10, the oscillatory curves of the first-order fields match well with each other, with nearly zero phase difference, since the first-order velocity is coupled with the first-order pressure in Eq. (6). In contrast, the second-order velocity field has a slight phase shift to the first-order fields, which can be attributed to the velocity gradient observed within the viscous boundary layer due to the no-slip boundary condition. A similar phase difference can be also seen in force fields and energy fields in Figs. 11 and 12.

According to Eqs. (12) and (15), the Stokes drag force is proportional to the second-order velocity ($\boldsymbol{F}_{drag} \propto \boldsymbol{v}_2$), while the radiation force is proportional to the acoustic pressure squared ($\boldsymbol{F}_{rad} \propto |p_1|^2$). From Eqs. (12)–(15), (28), and (29), the radiation force is scaled with the first-order average acoustic energy density, $\boldsymbol{F}_{rad} \propto \bar{E}_{tot}$, and the Stokes drag force is scaled with the second-order average kinetic energy density, $\boldsymbol{F}_{drag} \propto \sqrt{\bar{e}_{kin}}$. This enables us to theoretically establish the relationship between these physical fields and explain the similar phase difference. With respect to the scaling between physical fields, a higher amplitude of the first-order acoustofluidic fields will store more acoustic energy in the bulk volume, resulting in a stronger radiation force that drives particles toward the designated positions.

Based on the interference pattern of two wavefronts (as discussed in Sec. IV A 2) and the pseudo-standing wave in vertical direction (as discussed in Sec. III A), we can pinpoint the specific channel heights

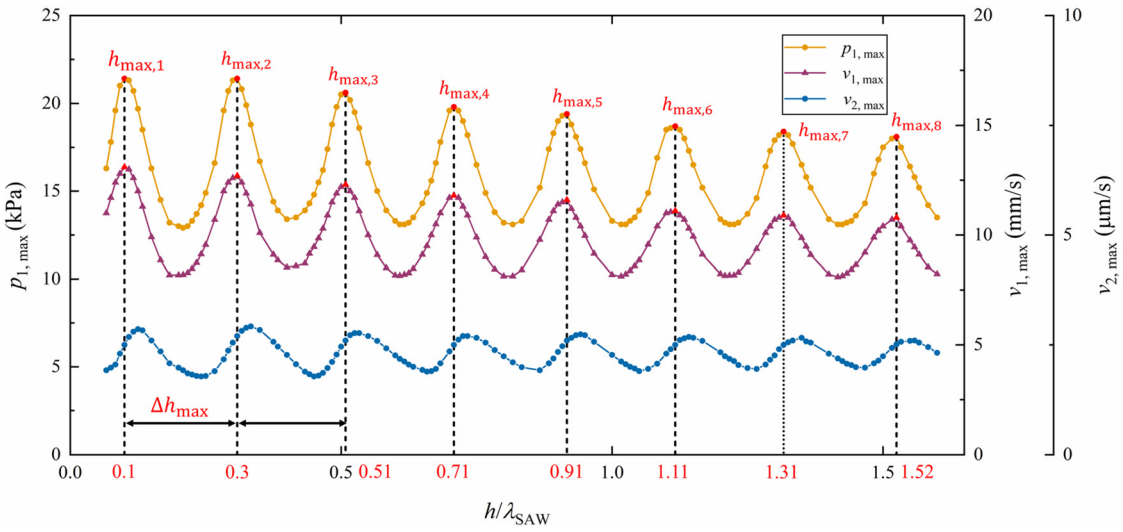

FIG. 10. Amplitude of the acoustofluidic fields, including the first-order pressure, the first-order velocity, and the second-order velocity.

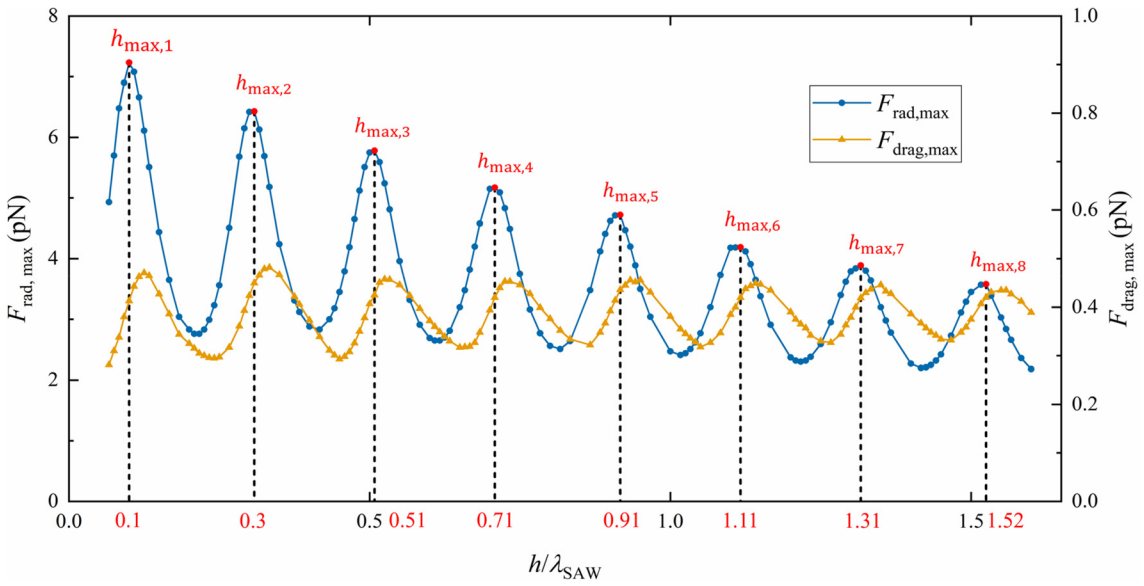

FIG. 11. Amplitude of the force fields, including the radiation force and the Stokes drag force.

that maximize acoustic pressure amplitude. These specific channel heights occur precisely when the first global pressure AN is situated at the actuation boundary (i.e., $z = 0$), as shown in Fig. 7(a). Therefore, we can derive these channel heights as

$$h_{max,n} = (2n-1)\frac{\lambda_\perp}{4}, \tag{30}$$

where n is an integer and $h_{max,n}$ is a function of $\lambda_\perp$. As we have known, $\lambda_f/\lambda_{SAW} = c_0/c_{sub}$. Substituting this relationship and Eq. (27) into Eq. (30) yields

$$h_{max,n} = \frac{(2n-1)\tan\left(\sin^{-1}\frac{c_0}{c_{sub}}\right)}{4}\lambda_{SAW}. \tag{31}$$

Hence, $h_{max,n}$ is further derived to be a function of λ_{SAW}. Such a relationship holds true for channels with width $W = \lambda_{SAW}$. The channel heights $h_{max,n}$ obtained in the numerical simulation are highlighted by red dots, and the corresponding values are labeled below the horizontal axis in Figs. 10–12. As shown in Fig. 13, the theoretical and numerical predictions of Δh_{max} are compared for different acoustic wavelengths

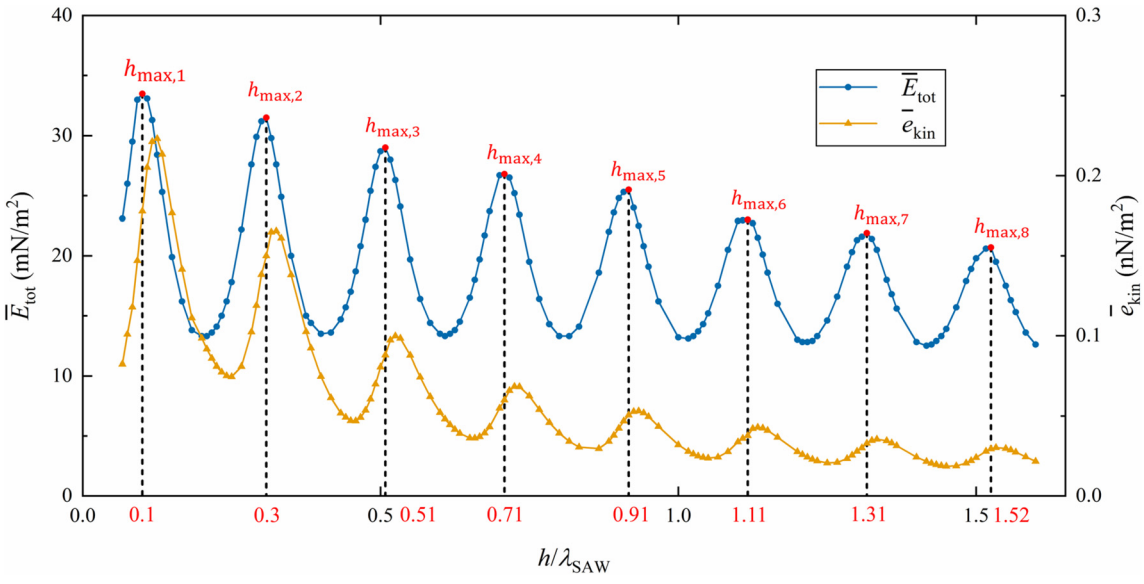

FIG. 12. Spatial average of the energy fields, including the average total acoustic energy density of the first-order fields and the average kinetic energy density of the second-order fields.

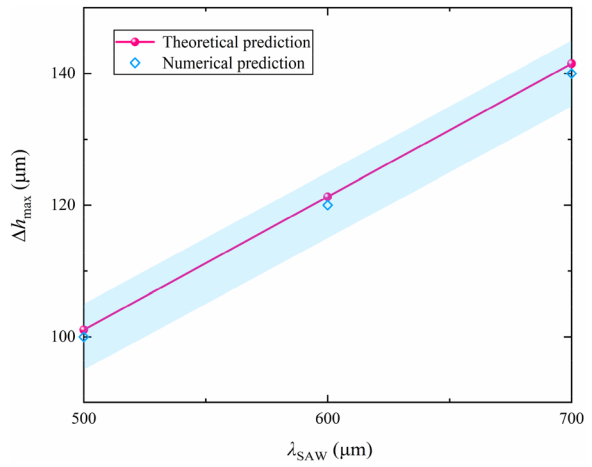

FIG. 13. Channel height intervals between adjacent pressure maxima for different λ_{SAW}.

λ_{SAW}. The theoretical values are calculated based on Eq. (30): $\Delta h_{max} = h_{max,n+1} - h_{max,n} = \lambda_{\perp}/2$. The channel height intervals Δh_{max} determined from numerical simulations are depicted in Fig. 10. These intervals are subsequently averaged and displayed in Fig. 13, facilitating a direct comparison with theoretical predictions. The blue band depicts the channel height increment in numerical simulations, i.e., $h_{step} = 5\,\mu$m. We vary the acoustic wavelength to better validate our hypothesis and find that our numerical prediction agrees well with the theoretical prediction for all the tested wavelengths, with all theoretical predictions within the error band.

B. Influences on acoustophoresis

Various performance metrics have been applied to assess the influence of design and operational parameters on particle aggregation, including purity, yield, aggregation efficiency, percentage of stuck particles, aggregation time, and sensitivity of particle size.[16] In each simulation, we simulate the particle trajectories with a uniform particle size, rendering the purity indicator not applicable. Moreover, the channel height is the only independent variable and has little impact on the cellular structure of the pressure distribution, resulting in almost all particles with a radius larger than the critical radius to eventually move into the target boxes. Therefore, yield and aggregation efficiency are not considered. Since the particle clogging phenomena are mainly observed in the streamwise direction, the percentage of stuck particles is not considered in our study. Therefore, we hereby consider the aggregation time and sensitivity of particle size as primary metrics to evaluate the performance of particle aggregation.

1. Aggregation timescale

The time required for all particles to aggregate in the target boxes t_a is a crucial parameter from a practical perspective, as shorter aggregation time can potentially reduce the device footprint by achieving higher throughput or shorter device length. Hence, we have determined the timescale for a complete particle aggregation at different channel heights, ranging from 40 to 960 μm, and identified the optimum channel height based on rapid aggregation. The timescale of particle aggregation can vary depending on channel geometry, device configuration, excitation frequency and power, liquid property, etc. For instance, faster aggregation can be achieved by increasing the displacement amplitude u_0 to obtain higher values of acoustic pressure amplitude and forces. Although the time required for particles to be fully aggregated in real applications may differ from our simulation results due to different setups, our findings are still useful in elucidating the relationship between the timescale of aggregation and the only independent variable in our study—the height of the channel. The radius of the polystyrene particle is fixed at 10 μm, which is greater than the critical radius. The displacement amplitude of the excited SAWs, u_0, is 0.1 nm.

Figure 14 shows the numerically predicted timescale of aggregation, t_a, as a function of the channel height, h. Red dots depict the optimum channel heights, h_{opt}, corresponding to the most efficient aggregation with the shortest aggregation time. We specify these optimum heights with red numbers below the horizontal axis, within 5 μm margin of error. The optimum heights occur periodically at intervals of around 120–125 μm, which can be attributed to the periodic variation of the magnitude of the resultant physical fields with the channel height, as discussed in Sec. IV A. The optimum heights can reduce the aggregation time by a maximum of 76% (100 s at $h = 110\,\mu$m vs 23 s at $h = 60\,\mu$m) and by a minimum of 43% (47 s at $h = 845\,\mu$m vs 27 s at $h = 910\,\mu$m) compared to the smallest aggregation time. As the channel height increases, the reduction in the aggregation time diminishes due to the oscillatory decay of the physical fields (Figs. 10–12). Notably, the amplitude of the first-order acoustic field, the radiation force field, and the average acoustic energy density reach their peaks at exactly the optimum heights. From Sec. IV A 3, the stronger acoustic field and radiation force lead to a greater amount of acoustic energy contained in the bulk volume, which gives rise to the faster particle aggregation. In addition, at channel heights $h = h_{max,n}$, the specific radiation force pushes the near-bottom particles away, as illustrated by the bottom panel of Fig. 8(a), which prevents particles from being trapped within the bottom-driven acoustic streaming cell and therefore contributes to the reduction in aggregation time. Conversely, in cases where the channel height deviates from $h_{max,n}$, the radiation force pushes the near-bottom particles toward the bottom wall, as depicted in the top panel of Fig. 8(a), trapping particles within the streaming-dominated areas. Therefore, the dimensionless optimum heights of the soft-walled microchannel for the SSAW-based particle aggregation device are determined as follows:

$$h^*_{opt} = \frac{h_{opt}}{\lambda_{SAW}} = \frac{h_{max,n}}{\lambda_{SAW}} = \frac{(2n-1)\tan\left(\sin^{-1}\frac{c_0}{c_{sub}}\right)}{4}. \quad (32)$$

For SAWs traveling at the surface of the $LiNbO_3$ substrate and channels filled with water, Eq. (32) can be further simplified as $h^*_{opt} \approx 0.101\,07 \cdot (2n-1)$. Since the channel height and width are proportional to the acoustic wavelength λ_{SAW}, the underlying relationships are expected to hold true for all acoustic frequencies. To further test our hypothesis, we define the dimensionless difference between the optimum channel height predicted by Eq. (32) (denoted by $h_{opt,th}$) and the numerical predicted value (denoted by $h_{opt,nu}$) as $\Delta h^* = (h_{opt,nu} - h_{opt,th})/h_{opt,th}$. In Fig. 15, Δh^* is plotted against the integer n for various side lengths of the target box l, displacement amplitude u_0, and particle radii r, revealing that the difference between

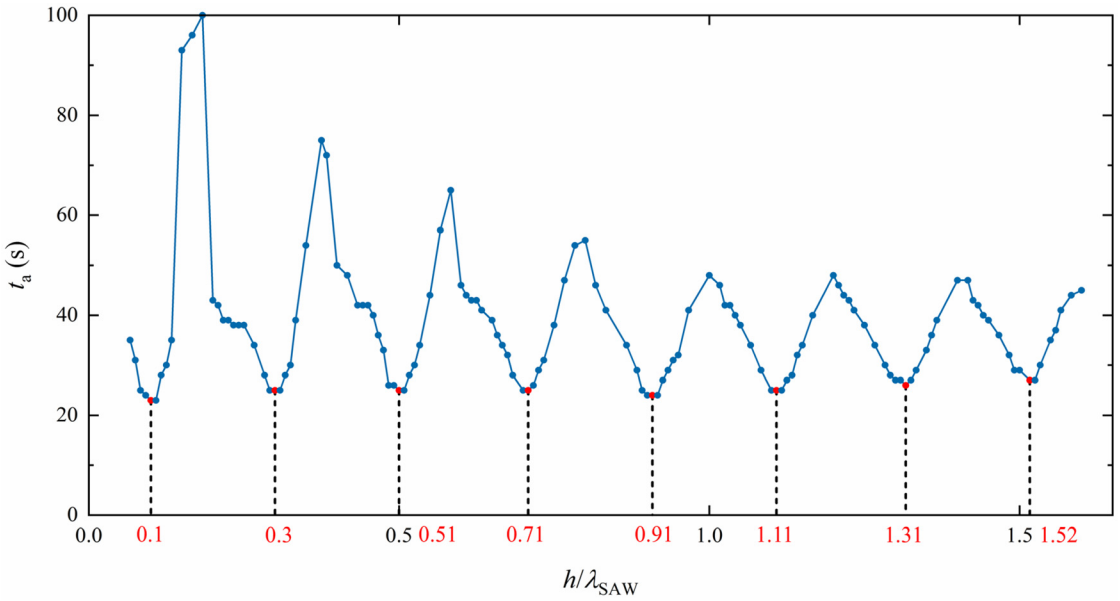

FIG. 14. Timescale for particle aggregation at different channel heights.

the theoretical and numerical predictions is less than 2% for all cases. Hence, the optimum channel height for a rapid particle aggregation can be determined by Eq. (32), irrespective of the size of the target box, displacement amplitude, and particle size.

2. Sensitivity of particle size

In this section, the sensitivity of particle aggregation to particle size at various channel heights is studied. Based on the different scaling relationships of forces with particle radius ($\boldsymbol{F}_{\mathbf{rad}} \propto r^3$ and $\boldsymbol{F}_{\mathbf{drag}} \propto r$) according to Eqs. (12) and (15), we conduct extensive numerical simulations with particle radii ranging from 0.5 to 10 μm to determine the critical particle size, r_{crit}, which denotes the threshold between the drag-force-dominance regime and the radiation-force-dominance regime, at different channel heights ranging from 40 to 960 μm. Representative resultant particle trajectories are shown in Fig. 16 for channel heights of 120 and 540 μm, respectively. We find that the critical particle radius, r_{crit}, is consistently around 5–6 μm for all the channel heights examined. The acoustophoretic aggregation is dependent on the particle size, where 0.5 μm particles undergo looping within the acoustic streaming vortices due to the dominance of the viscous drag force [Fig. 16(a)], while 5 μm particles move toward PNs driven by the radiation force [Fig. 16(d)]. It is noteworthy that particle aggregation exhibits a spatially dependent feature at certain particle sizes when the channel height is larger than a quarter of the SAW wavelength ($h > \lambda_{SAW}/4 = 150\ \mu$m), as shown in Figs. 16(b) and 16(c). When the particle radius is 1.5 μm, particles in the upper region of the channel ($z > \lambda_{SAW}/4 = 150\ \mu$m) start to move toward PNs, while particles in the bottom region of the channel ($z < \lambda_{SAW}/4 = 150\ \mu$m) always remain in circulation in the streaming vortices and gradually aggregate toward the centers of the vortices, as shown in Fig. 16(b). As the particle radius increases to 3 μm, this spatially dependent particle aggregation pattern becomes more pronounced, with the majority of particles either aggregating into the target boxes or concentrating at the centers of the four streaming vortices in a short period [Fig. 16(c)]. Once the particle size is larger than 5 μm, this spatially dependent pattern disappears, leaving identical aggregation pattern over the entire cross section, as shown in Fig. 16(d).

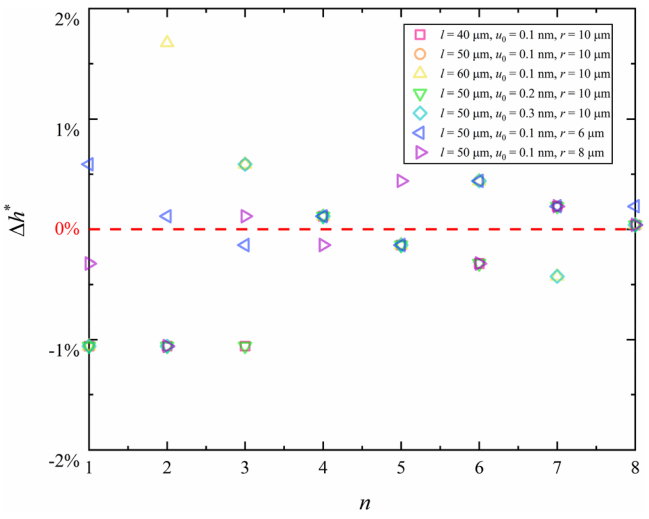

FIG. 15. Dimensionless difference between theoretical and numerical predictions of optimum channel heights for various target box sizes, displacement amplitude, and particle radii.

To better understand the mechanisms of such spatially dependent particle movement, we investigate the particle velocity components, including radiation force component $\boldsymbol{v}_{\mathbf{rad}} = \boldsymbol{F}_{\mathbf{rad}}/6\pi\mu r$ and the

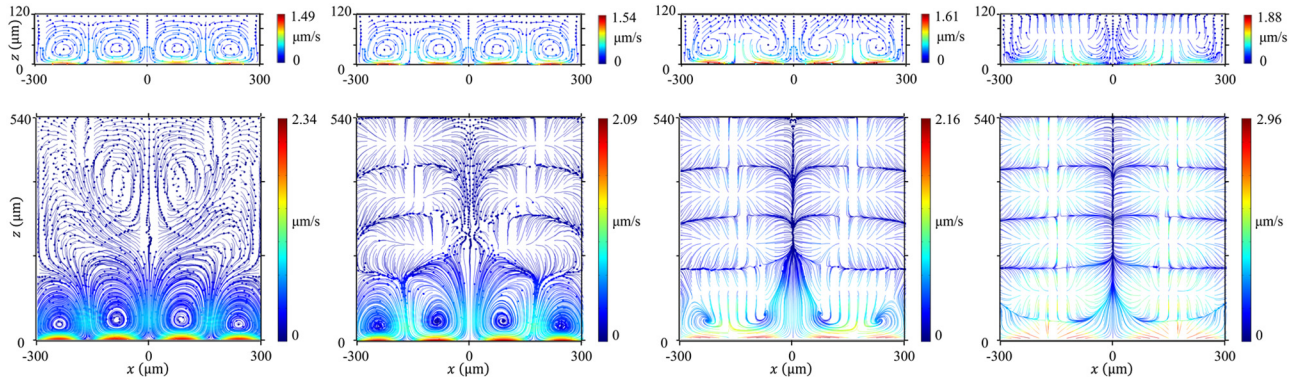

FIG. 16. Particle trajectories at channel heights $h = 120$ and 540 μm for particle radii of (a) 0.5, (b) 1.5, (c) 3, and (d) 5 μm. The magnitude of the particle speed is denoted by the colors ranging from blue, as for the minimum, to red, as for the maximum.

streaming component $\boldsymbol{v}_2$ according to Eq. (17). Figure 17 shows the discrepancy between the two particle components $\boldsymbol{v}_{\mathbf{d}} = \boldsymbol{v}_{\mathbf{rad}} - \boldsymbol{v}_2$ for channel heights of 125 and 540 μm. For the case of $h = 125$ μm, the particle velocity is dominated by $\boldsymbol{v}_2$ when $r < 5$ μm or by $\boldsymbol{v}_{\mathbf{rad}}$ when $r \geq 5$ μm. In contrast, for the case of $h = 540$ μm, spatial dominance of different particle velocity components over the cross section is observed when $1.5\,\mu\text{m} \leq r \leq 5\,\mu\text{m}$. With the particle radius of 1.5 μm, the influence of $\boldsymbol{v}_{\mathbf{rad}}$ starts to enhance and dominates the upper region of the channel, while $\boldsymbol{v}_2$ still dominates over $\boldsymbol{v}_{\mathbf{rad}}$ near the bottom, as shown in Figs. 17(b) and 17(c). This can be attributed to the confined influences of the second-order streaming field $\boldsymbol{v}_2$ and its kinetic energy $\bar{e}_{\text{kin}}$ within a quarter of the SAW wavelength above the bottom boundary. The spatial dominance of different particle velocity components leads to the spatially dependent particle aggregation pattern observed in Figs. 16(b) and 16(c). Once the particle radius reaches 5 μm, the dominance of $\boldsymbol{v}_{\mathbf{rad}}$ over $\boldsymbol{v}_2$ spans the entire channel [Fig. 17(d)], resulting in a uniform aggregation pattern [Fig. 16(d)]. Therefore, the spatially dependent particle aggregation occurs when the channel height is larger than $\lambda_{\text{SAW}}/4$ and the particle radius is around 1.5–5 μm.

V. CONCLUSIONS

We have established a 2D cross-sectional numerical model to investigate the characteristics of the flow fields and microparticle trajectories in rectangular PDMS channels actuated by two counter-propagating SAWs at the bottom. The numerical model has been validated against previous experimental and numerical results reported in the literature.

With the width of the channel fixed at the SAW wavelength of 600 μm, which corresponds to the SAW frequency of 6.65 MHz, the influences of the channel height on the performance of particle aggregation are studied by varying the channel height from 40 to 960 μm. We found that the spatial distributions of the first-order flow fields exhibit periodic variations in the vertical direction, while the

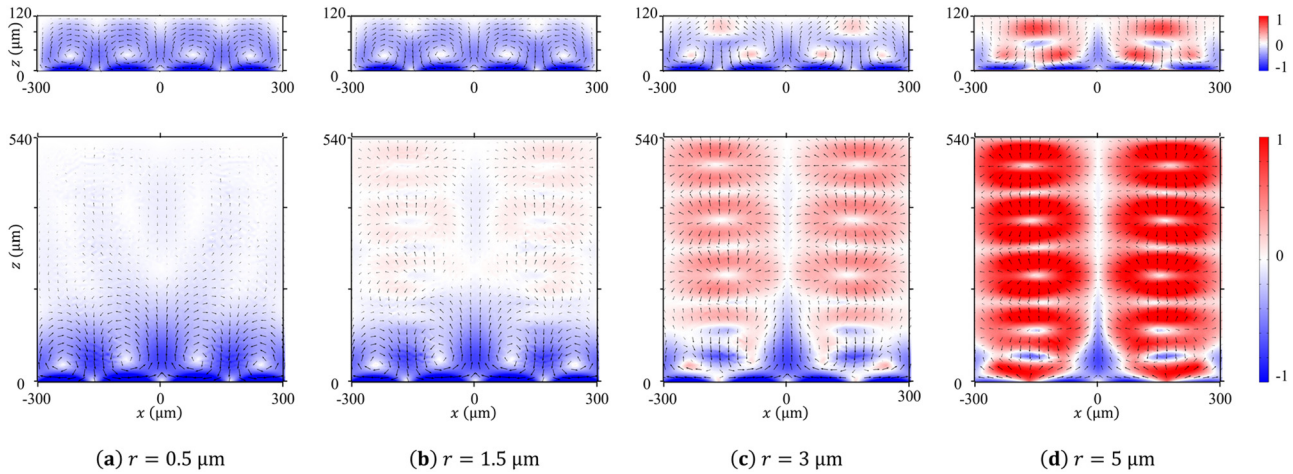

FIG. 17. Difference between the radiation force component and the streaming component of particle velocity at channel heights $h = 120$ and 540 μm for particle radii of (a) 0.5, (b) 1.5, (c) 3, and (d) 5 μm. The magnitude of the difference is denoted by red (radiation force component dominates), white (balance between two components), and blue (streaming component dominates). The vectors of the resultant particle velocity are shown as black arrows.

second-order flow fields are mainly confined near the bottom of the channel within a distance equal to a quarter of the SAW wavelength. Through investigating the physical mechanism of the SAW propagation, we determined the vertical wavelength of the interference pattern $\lambda_\perp$. The strength of the physical fields within the channel varies with the channel height in an oscillatory decay fashion, and the peak value reoccurs at the interval of $\lambda_\perp/2$. A phase difference is observed between the oscillations of the first-order fields and the oscillations of the second-order fields.

The optimum channel heights for rapid microparticle aggregation can be summarized to be $(2n-1)\tan\left(\sin^{-1}c_0/c_{\text{sub}}\right)/4$. High acoustic pressure, strong radiation force, and large acoustic energy are produced at these optimum heights, enabling acoustofluidic devices to achieve more efficient particle manipulation.

Furthermore, we simulated the particle trajectories with radii ranging from 0.5 to 10 μm. The critical particle radius was found to be around 5∼6 μm, irrespective of the channel height. When the channel height is larger than a quarter of the SAW wavelength, particle aggregation demonstrates a spatial-dependence pattern for particle radii of 1.5–5 μm. Particles in the lower region of the channel ($z < \lambda_{\text{SAW}}/4$) circulate and finally concentrate toward the centers of the streaming vortices driven by the drag force, while particles in the upper region of the channel ($z > \lambda_{\text{SAW}}/4$) aggregate toward PNs under the dominant influence of the radiation force.

Our investigations have shed light on the underlying physical mechanism of acoustophoresis and gained valuable insight into the optimum design of acoustofluidic microchannels.

ACKNOWLEDGMENTS

The work has been supported by the Energy IRC Small Grants scheme funded by the Isaac Newton Trust/Energy Policy Research Group (EPRG) and the NERC Discipline Hopping for Environmental Solutions initiative. For the purpose of open access, the authors have applied a Creative Commons Attribution (CC BY) license to any Author Accepted Manuscript version arising from this submission.

AUTHOR DECLARATIONS

Conflict of Interest

The authors have no conflicts to disclose.

Author Contributions

Yiming Li: Conceptualization (equal); Formal analysis (equal); Methodology (equal); Software (lead); Visualization (equal); Writing – original draft (lead). **Dongfang Liang:** Conceptualization (equal); Formal analysis (equal); Funding acquisition (lead); Resources (equal); Software (supporting); Supervision (lead); Visualization (equal); Writing – review & editing (lead). **Alexandre J. Kabla:** Visualization (equal); Writing – review & editing (supporting). **Yuning Zhang:** Visualization (equal); Writing – review & editing (supporting). **Xin Yang:** Resources (equal); Visualization (equal); Writing – review & editing (supporting).

DATA AVAILABILITY

The data that support the findings of this study are available from the corresponding author upon reasonable request.

REFERENCES

[1]S. Zhang, Y. Wang, P. Onck, and J. den Toonder, "A concise review of microfluidic particle manipulation methods," Microfluid. Nanofluid. **24**(4), 24 (2020).
[2]H. Yun, K. Kim, and W. G. Lee, "Cell manipulation in microfluidics," Biofabrication **5**(2), 022001 (2013).
[3]L. Y. Yeo and J. R. Friend, "Surface acoustic wave microfluidics," Annu. Rev. Fluid Mech. **46**, 379–406 (2014).
[4]X. Ding, P. Li, S.-C. S. Lin, Z. S. Stratton, N. Nama, F. Guo, D. Slotcavage, X. Mao, J. Shi, F. Costanzo, and T. J. Huang, "Surface acoustic wave microfluidics," Lab Chip **13**(18), 3626 (2013).
[5]B. Zhang, W. Zhao, D. Yuan, T. Wang, and W. Wu, "A novel microparticle size sorting technology based on sheath flow stable expansion regimes," Phys. Fluids **35**(5), 052018 (2023).
[6]B. Zhang, W. Wu, Q. Zhao, and S. Yan, "Geometric optimization of double layered microchannel with grooves array for enabling nanoparticle manipulation," Phys. Fluids **35**(6), 062009 (2023).
[7]J. Rufo, F. Cai, J. Friend, M. Wiklund, and T. J. Huang, "Acoustofluidics for biomedical applications," Nat. Rev. Methods Primers **2**(1), 30 (2022).
[8]M. Wu, A. Ozcelik, J. Rufo, Z. Wang, R. Fang, and T. Jun Huang, "Acoustofluidic separation of cells and particles," Microsyst. Nanoeng. **5**(1), 32 (2019).
[9]N. Nama, R. Barnkob, Z. Mao, C. J. Kähler, F. Costanzo, and T. J. Huang, "Numerical study of acoustophoretic motion of particles in a PDMS microchannel driven by surface acoustic waves," Lab Chip **15**(12), 2700–2709 (2015).
[10]M. Gedge and M. Hill, "Acoustofluidics 17: Theory and applications of surface acoustic wave devices for particle manipulation," Lab Chip **12**(17), 2998 (2012).
[11]E. Taatizadeh, A. Dalili, P. I. Rellstab-Sánchez, H. Tahmooressi, A. Ravishankara, N. Tasnim, H. Najjaran, I. T. S. Li, and M. Hoorfar, "Micron-sized particle separation with standing surface acoustic wave—Experimental and numerical approaches," Ultrason. Sonochem. **76**, 105651 (2021).
[12]S. Zhao, Z. Liu, Y. Ren, N. Zheng, R. Chen, F. Cai, and Y. Pang, "Study of micro-scale flow characteristics under surface acoustic waves," Phys. Fluids **35**(8), 082011 (2023).
[13]Y. Gu, C. Chen, Z. Mao, H. Bachman, R. Becker, J. Rufo, Z. Wang, P. Zhang, J. Mai, S. Yang, J. Zhang, S. Zhao, Y. Ouyang, D. T. W. Wong, Y. Sadovsky, and T. J. Huang, "Acoustofluidic centrifuge for nanoparticle enrichment and separation," Sci. Adv. **7**(1), eabc0467 (2021).
[14]S. Xue, Q. Xu, Z. Xu, X. Zhang, H. Zhang, X. Zhang, F. He, Y. Chen, Y. Xue, and P. Hao, "Manipulation of particle/cell based on compressibility in a divergent microchannel by surface acoustic wave," Anal. Chem. **95**, 4282 (2023).
[15]W. Qiu, H. Bruus, and P. Augustsson, "Particle-size-dependent acoustophoretic motion and depletion of micro- and nano-particles at long timescales," Phys. Rev. E **102**(1), 013108 (2020).
[16]M. A. Şahin, B. Çetin, and M. B. Özer, "Investigation of effect of design and operating parameters on acoustophoretic particle separation via 3D device-level simulations," Microfluid. Nanofluid. **24**(1), 8 (2019).
[17]S. Marefati, M. Ghassemi, and V. Ghazizadeh, "Investigation of effective parameters on streaming-induced acoustophoretic particle manipulation in a microchannel via three-dimensional numerical simulation," Phys. Fluids **34**(1), 012008 (2022).
[18]P. B. Muller, R. Barnkob, M. J. H. Jensen, and H. Bruus, "A numerical study of microparticle acoustophoresis driven by acoustic radiation forces and streaming-induced drag forces," Lab Chip **12**(22), 4617 (2012).
[19]C. Devendran, T. Albrecht, J. Brenker, T. Alan, and A. Neild, "The importance of travelling wave components in standing surface acoustic wave (SSAW) systems," Lab Chip **16**(19), 3756–3766 (2016).
[20]C. Devendran, D. J. Collins, and A. Neild, "The role of channel height and actuation method on particle manipulation in surface acoustic wave (SAW)-driven microfluidic devices," Microfluid. Nanofluid. **26**(2), 9 (2022).
[21]S. Sachs, M. Baloochi, C. Cierpka, and J. König, "On the acoustically induced fluid flow in particle separation systems employing standing surface acoustic waves—Part I," Lab Chip **22**(10), 2011–2027 (2022).
[22]J. Dong, D. Liang, X. Yang, and C. Sun, "Influences of microparticle radius and microchannel height on SSAW-based acoustophoretic aggregation," Ultrasonics **117**, 106547 (2021).

[23]H. Wang, F. Yuan, Z. Xie, C. Sun, F. Wu, R. Mikhaylov, M. Shen, J. Yang, Y. Zhou, D. Liang, X. Sun, Z. Wu, Z. Yang, and X. Yang, "Modelling hybrid acoustofluidic devices for enhancing nano- and micro-particle manipulation in microfluidics," Appl. Acoust. **205**, 109258 (2023).
[24]Y. Wu, A. G. Stewart, and P. V. S. Lee, "High-throughput microfluidic compressibility cytometry using multi-tilted-angle surface acoustic wave," Lab Chip **21**(14), 2812–2824 (2021).
[25]J.-C. Hsu and C.-L. Chao, "Full-wave modeling of micro-acoustofluidic devices driven by standing surface acoustic waves for microparticle acoustophoresis," J. Appl. Phys. **128**(12), 124502 (2020).
[26]L. Liu, J. Zhou, K. Tan, H. Zhang, X. Yang, H. Duan, and Y. Fu, "A simplified three-dimensional numerical simulation approach for surface acoustic wave tweezers," Ultrasonics **125**, 106797 (2022).
[27]X. Liu, T. Zheng, and C. Wang, "Three-dimensional modeling and experimentation of microfluidic devices driven by surface acoustic wave," Ultrasonics **129**, 106914 (2023).
[28]P. Kr. Das and V. R. Bhethanabotla, "Development of a thermo-pressure acoustic model and its application in modeling three-dimensional acoustofluidic systems," Phys. Fluids **35**(3), 036115 (2023).
[29]J. Friend and L. Y. Yeo, "Microscale acoustofluidics: Microfluidics driven via acoustics and ultrasonics," Rev. Mod. Phys. **83**(2), 647–704 (2011).
[30]H. Bruus, "Acoustofluidics 1: Governing equations in microfluidics," Lab Chip **11**(22), 3742 (2011).
[31]R. Barnkob, N. Nama, L. Ren, T. J. Huang, F. Costanzo, and C. J. Kähler, "Acoustically driven fluid and particle motion in confined and leaky systems," Phys. Rev. Appl. **9**(1), 014027 (2018).
[32]D. Köster, "Numerical simulation of acoustic streaming on surface acoustic wave-driven biochips," SIAM J. Sci. Comput. **29**(6), 2352–2380 (2007).
[33]M. Settnes and H. Bruus, "Forces acting on a small particle in an acoustical field in a viscous fluid," Phys. Rev. E **85**(1), 016327 (2012).
[34]H. Bruus, "Acoustofluidics 7: The acoustic radiation force on small particles," Lab Chip **12**(6), 1014 (2012).
[35]L. D. Landau, E. M. Lifshitz, J. B. Sykes, W. H. Reid, and E. H. Dill, "Theory of elasticity: Vol. 7 of course of theoretical physics," Phys. Today **13**(7), 44–46 (1960).
[36]H. Bruus, *Theoretical Microfluidics* (Oxford University Press, Oxford, New York, 2007).
[37]C. Jin, C. Ma, Z. Yang, and H. Lin, "A force measurement method based on flexible PDMS grating," Appl. Sci. **10**(7), 2296 (2020).
[38]C. Devendran, D. J. Collins, Y. Ai, and A. Neild, "Huygens–Fresnel acoustic interference and the development of robust time-averaged patterns from traveling surface acoustic waves," Phys. Rev. Lett. **118**(15), 154501 (2017).
[39]H. G. Kraus, "Huygens–Fresnel–Kirchhoff wave-front diffraction formulation: Spherical waves," J. Opt. Soc. Am. A **6**(8), 1196 (1989).
[40]N. Skov and H. Bruus, "Modeling of microdevices for SAW-based acoustophoresis—A study of boundary conditions," Micromachines **7**(10), 182 (2016).
[41]D. R. Lide, G. Baysinger, S. Chemistry, L. I. Berger, R. N. Goldberg, and H. V. Kehiaian, *CRC Handbook of Chemistry and Physics, Internet Version 2005* (CRC Press, Boca Raton, FL, 2005).
[42]L. Bergmann, *Der Ultraschall Und Seine Anwendung in Wissenschaft Und Technik* (S. Hirzel Verlag, Stuttgart, 1954).
[43]M. J. Holmes, N. G. Parker, and M. J. W. Povey, "Temperature dependence of bulk viscosity in water using acoustic spectroscopy," J. Phys. **269**, 012011 (2011).
[44]D. Armani, C. Liu, and N. R. Aluru, "Re-configurable fluid circuits by PDMS elastomer micromachining," in *12th IEEE International Conference on Micro Electro Mechanical Systems (MEMS)* (IEEE, 1999), pp. 222–227.
[45]I. Kuznetsova, I. Nedospasov, A. Smirnov, V. Anisimkin, D. Roshchupkin, M.-A. Signore, L. Francioso, J. Kondoh, M. Serebrov, V. Kashin, and V. Kolesov, "The peculiarities of the acoustic waves of zero-order focusing in lithium niobate plate," Sensors **21**(12), 4000 (2021).
[46]H. Bruus, "Acoustofluidics 2: Perturbation theory and ultrasound resonance modes," Lab Chip **12**(1), 20–28 (2012).
[47]A. Gantner, R. H. W. Hoppe, D. Köster, K. Siebert, and A. Wixforth, "Numerical simulation of piezoelectrically agitated surface acoustic waves on microfluidic biochips," Comput. Visualization Sci. **10**(3), 145–161 (2007).
[48]R. M. Arzt, E. Salzmann, and K. Dransfeld, "Elastic surface waves in quartz at 316 MHz," Appl. Phys. Lett. **10**(5), 165–167 (1967).
[49]Z. Mao, Y. Xie, F. Guo, L. Ren, P.-H. Huang, Y. Chen, J. Rufo, F. Costanzo, and T. J. Huang, "Experimental and numerical studies on standing surface acoustic wave microfluidics," Lab Chip **16**(3), 515–524 (2016).
[50]D. J. Collins, R. O'Rorke, A. Neild, J. Han, and Y. Ai, "Acoustic fields and microfluidic patterning around embedded micro-structures subject to surface acoustic waves," Soft Matter **15**(43), 8691–8705 (2019).